SANDIA REPORT

SAND2010-6446
Unlimited Release
Printed September 2010

Quantifying the Debonding of Inclusions Through Tomography and Computational Homology

Alejandro Mota, Huiqing Jin, Wei-Yang Lu, James W. Foulk III, George C. Johnson

Prepared by
Sandia National Laboratories
Albuquerque, New Mexico 87185 and Livermore, California 94550

Sandia National Laboratories is a multi-program laboratory managed and operated by Sandia Corporation, a wholly owned subsidiary of Lockheed Martin Corporation, for the U.S. Department of Energy's National Nuclear Security Administration under contract DE-AC04-94AL85000.

Approved for public release; further dissemination unlimited.

Sandia National Laboratories

Issued by Sandia National Laboratories, operated for the United States Department of Energy by Sandia Corporation.

NOTICE: This report was prepared as an account of work sponsored by an agency of the United States Government. Neither the United States Government, nor any agency thereof, nor any of their employees, nor any of their contractors, subcontractors, or their employees, make any warranty, express or implied, or assume any legal liability or responsibility for the accuracy, completeness, or usefulness of any information, apparatus, product, or process disclosed, or represent that its use would not infringe privately owned rights. Reference herein to any specific commercial product, process, or service by trade name, trademark, manufacturer, or otherwise, does not necessarily constitute or imply its endorsement, recommendation, or favoring by the United States Government, any agency thereof, or any of their contractors or subcontractors. The views and opinions expressed herein do not necessarily state or reflect those of the United States Government, any agency thereof, or any of their contractors.

Printed in the United States of America. This report has been reproduced directly from the best available copy.

Available to DOE and DOE contractors from
U.S. Department of Energy
Office of Scientific and Technical Information
P.O. Box 62
Oak Ridge, TN 37831

Telephone:	(865) 576-8401
Facsimile:	(865) 576-5728
E-Mail:	reports@adonis.osti.gov
Online ordering:	http://www.osti.gov/bridge

Available to the public from
U.S. Department of Commerce
National Technical Information Service
5285 Port Royal Rd
Springfield, VA 22161

Telephone:	(800) 553-6847
Facsimile:	(703) 605-6900
E-Mail:	orders@ntis.fedworld.gov
Online ordering:	http://www.ntis.gov/help/ordermethods.asp?loc=7-4-0#online

SAND2010-6446
Unlimited Release
Printed September 2010

Quantifying the Debonding of Inclusions Through Tomography and Computational Homology

Alejandro Mota, Huiqing Jin, Wei-Yang Lu, James W. Foulk III
Sandia National Laboratories
Livermore, CA 94551
amota@sandia.gov

George C. Johnson
University of California, Berkeley
Berkeley, CA 94720
gjohnson@me.berkeley.edu

Abstract

This report describes a Laboratory Directed Research and Development (LDRD) project to use of synchrotron-radiation computed tomography (SRCT) data to determine the conditions and mechanisms that lead to void nucleation in rolled alloys.

The Advanced Light Source (ALS) at Lawrence Berkeley National Laboratory (LBNL) has provided SRCT data of a few specimens of 7075-T7351 aluminum plate (widely used for aerospace applications) stretched to failure, loaded in directions perpendicular and parallel to the rolling direction. The resolution of SRCT data is 900nm, which allows elucidation of the mechanisms governing void growth and coalescence.

This resolution is not fine enough, however, for nucleation. We propose the use statistics and image processing techniques to obtain sub-resolution scale information from these data, and thus determine where in the specimen and when during the loading program nucleation occurs and the mechanisms that lead to it.

Quantitative analysis of the tomography data, however, leads to the conclusion that the reconstruction process compromises the information obtained from the scans. Alternate, more powerful reconstruction algorithms are needed to address this problem, but those fall beyond the scope of this project.

Acknowledgments

We gratefully acknowledge the support of the Advanced Light Source at Lawrence Berkeley National Laboratory, and in particular Alastair MacDowell and Dula Parkinson at the 8.3.2 tomography beamline. Support for this project was provided by Sandia's Laboratory Directed Research and Development (LDRD) program.

Contents

1 Introduction **11**

1.1 Outline 11

2 The Experiment **13**

2.1 Anisotropic Behavior 13

2.2 The Specimens 16

3 Tomography and Reconstruction **21**

3.1 Tomographic Scan 21

3.2 The Reconstruction Process 21

3.3 Reconstruction from Sampled Data 23

4 Quantitative Analysis of Tomography Data **25**

4.1 Distribution of Attenuation in Scans 25

4.2 Separation of Voids and Particles 31

4.3 Extraction of Under-Resolved Information 35

4.4 Error in Reconstruction 38

5 Conclusion **43**

References **44**

List of Figures

2.1 Four notched tensile specimens for the characterization of failure in ductile metals. 14

2.2 Load vs. displacement for R3 specimens of 7075-T7351 aluminum. 15

2.3 Reconstructed cross section near the failure surface of a transverse specimen of 7075-T7351 aluminum. 16

2.4 Loading programs and directions with scan indicators: (a) Smooth specimen, longitudinal (L); (b) Smooth specimen, long transverse (T); (c) Smooth specimen, short transverse (S); (d) Notched specimen, longitudinal (L). 18

4.1 Typical section of reconstructed images for smooth transverse (T) specimen near the center: (a) ST1, near intact; (b) ST5, void growth; (c) ST6, coalescence and rupture. 26

4.2 NL4 scan near the center of the specimen. Dark areas are voids and bright areas are particles. Diameter of specimen is 1.27mm 27

4.3 Normalized distribution of aluminum matrix attenuation values ($\mu = 0$, $\sigma = 1$) compared with the normal distribution N(0,1). 28

4.4 Distribution of attenuation values outside specimen for scan SS1. 29

4.5 Histogram of attenuation values for scan ST1: (a) linear-linear scale; (b) linear-log scale. 30

4.6 Identification of matrix normal distribution for scan ST1. Black, normal with μ and σ. Red, least-squares fit. Blue, RANSAC fit. Green, outlier distribution. (a) linear-linear scale; (b) linear-log scale. 34

4.7 Scan ST1 after applying separation criterion (4.11) with $p = 0.95$. Voxel size = 900nm (a) all outliers; (b) voids; (c) particles. 37

4.8 Evolution of void and particle volume fractions with loading: (a) NL Specimen; (b) SL Specimen; (c) SS Specimen; (d) ST Specimen. 40

4.9 Reconstruction Artifacts: (a) NL3 Scan; (b) SL4 Scan; (c) SS6 Scan; (d) ST1 Scan. 41

List of Tables

2.1 Scans and load levels. 19

4.1 Statistics for scan ST1. 27

4.2 Statistics for all scans. 32

4.3 Normal fits and void and particle thresholds for $p = 0.95$. 36

4.4 Void and particle volume fractions. 39

Chapter 1

Introduction

An accurate description of the kinetics of void nucleation, growth and coalescence is of paramount importance for the understanding of ductile fracture and failure in structural alloys. Over the years, many models have been proposed that rely on empirical and simplified assumptions for the modeling of these phenomena. These simplified models, however, are inadequate to model the evolution of anisotropic damage in rolled aluminum alloys. Thus, more detailed descriptions based on micro-mechanics are needed to model more accurately the processes that lead to failure and therefore obtain more reliable predictions.

Specimens of fractured aluminum alloy are imaged in-situ using Synchrotron-Radiation Computed Tomography (SRCT). This shows the attenuation to X-rays that is correlated to the density of the material, thus uncovering its internal structure. This is adequate to reveal the three-dimensional structure of inclusions and voids, and the mechanisms that lead to the formation of void chains, void sheets, and fracture surfaces. This information is crucial for developing a material model.

The resolution of SRCT is 900nm, which is insufficient for the determination of void nucleation mechanisms. Thus, we propose to analyze SRCT data using state-of-the-art tools of computational homology to determine the evolution of debonding. The computation of the Betti numbers is most relevant to the determination of whether interfaces are debonded or not: the first number B_1 is the number of connected components (fully debonded inclusions), B_2 is the numbers of tunnels (partially debonded inclusions), and B_3 is the number of isolated voids (fully formed voids) [9, 10].

As SRCT data is obtained about the loading of a particular specimen, we propose the use the tools of statistics and computational homology to track the evolution of the Betti numbers and therefore follow the evolution of the debonding of interfaces, and from this information understand the mechanisms that lead to void nucleation.

1.1 Outline

Chapter 2 addresses the motivation for the experiment, which is the anisotropic damage phenomenon observed in rolled aluminum allows. Based on this behavior, we propose a set of experiments to be performed at the Advanced Light Source. Chapter 3 describes the

tomographic scan and reconstruction processes. Finally, Chapter 4 describes the quantitative analysis performed on the data obtained from tomography and the results.

Chapter 2

The Experiment

We requested 144 hours and were granted 96 hours of time (48 hours starting 9:00am on July 13, 2010 and 48 hours starting 9:00am on November 10, 2010) on the micro-tomography beamline (beamline 8.3.2) at the Advanced Light Source at Lawrence Berkeley National Laboratory in order to investigate the evolution of micron-scale damage and the role of microstructural mechanisms during the large deformation of high strength aluminum alloys. These materials are of considerable commercial importance owing to the substantial increase in yield and failure strength as compared with other aluminum alloys. This strength increase, however, comes at the expense of decreased ductility and toughness. In order to use these materials to their full potential, it is critical that the mechanisms leading to failure be understood much more fully than is currently the case. There is a paucity of good microstructural data available to help identify the roles of initiation, growth and ultimate coalescence of defects leading to material failure. This lack of data has not stopped the development of failure models, most of which attempt to mimic the macroscopic response of the material through matching such measures as toughness or ultimate strain. The micro-tomography facility at beamline 8.3.2 provides a unique opportunity to greatly increase our understanding of failure of high strength materials.

2.1 Anisotropic Behavior

A typical geometry used in materials testing of ductile metals is the notched tensile specimen, in which a stress concentration is intentionally introduced through reducing the cross-section in the notch region. This geometry has been widely used because the configuration of the notch affects the stress triaxiality which is known to promote void growth [11]. Figure 2.1 shows four different geometries of decreasing severity, with specimen R1 inducing relatively high triaxiality (and hence increased void growth) and R4 inducing relatively low triaxiality. In addition to the differences in damage that can be introduced by specimen geometry, it has been observed that there can be large differences in ductility associated with specimen orientation (i.e., loading in the rolling, short transverse or long transverse directions of rolled plate), even in materials that do not exhibit much anisotropy in their elastic or plastic response. In many materials, the issue of inhomogeneity is also of concern.

Figure 2.2 shows typical load-displacement curves for geometry R3, clearly demonstrating

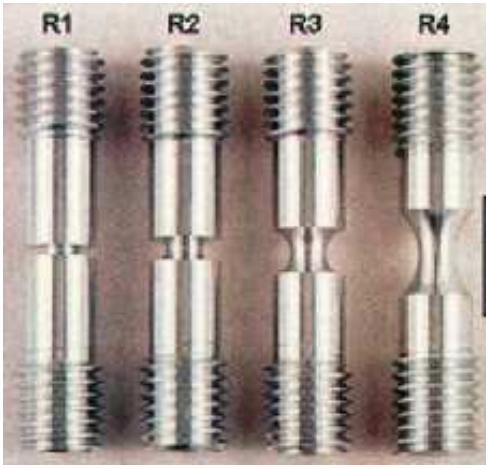

Figure 2.1. Four notched tensile specimens for the characterization of failure in ductile metals.

both the anisotropy and inhomogeneity that exists in this material (aluminum allow 7075-T7531). This material shows much more ductility in the rolling direction compared with either of the transverse directions, and the material at the surface exhibits greater strength, though this appears to have little influence on the ultimate ductility, as given by the strain to failure. Missing in these results is any understanding of the microstructure of the material and the manner in which this microstructure affects the initiation and growth of damage, ultimately leading to failure.

Preliminary experiments using the hard X-ray micro-tomography system on beamline 8.3.2 suggested that it is well suited to examine the microstructural characteristics of the material of interest: 7075 aluminum. Pure aluminum allows sufficient transmission of X-rays to permit high resolution of specimens that are on the order of millimeters thick. For example, at 30 keV the transmission through 2 mm pure aluminum is nearly 60% (associated with an attenuation length of 3.7 mm). In the 7XXX series of aluminum, a typical constituent (inclusion) particle that acts as a source of void nucleation is the intermetallic Al_7Cu_2Fe, which has an attenuation length of 0.7 mm. Thus, there is reasonable contrast between the matrix material and the inclusion particles. It is important to recognize, however, that there are other important microstructural inhomogeneities, such as dispersoids and precipitates, that are not visible through X-ray tomography because of their small size.

In order to determine whether these small microstructural features play a significant role in the failure mechanisms, we performed fractography of the failure surfaces and scanning electron microscopy (SEM) on sectioned specimens after they were examined with X-ray tomography.

As an initial proof of concept, two fractured specimens were examined on beamline 8.3.2 by ALS scientists in November 2009. The results were extremely encouraging that the pro-

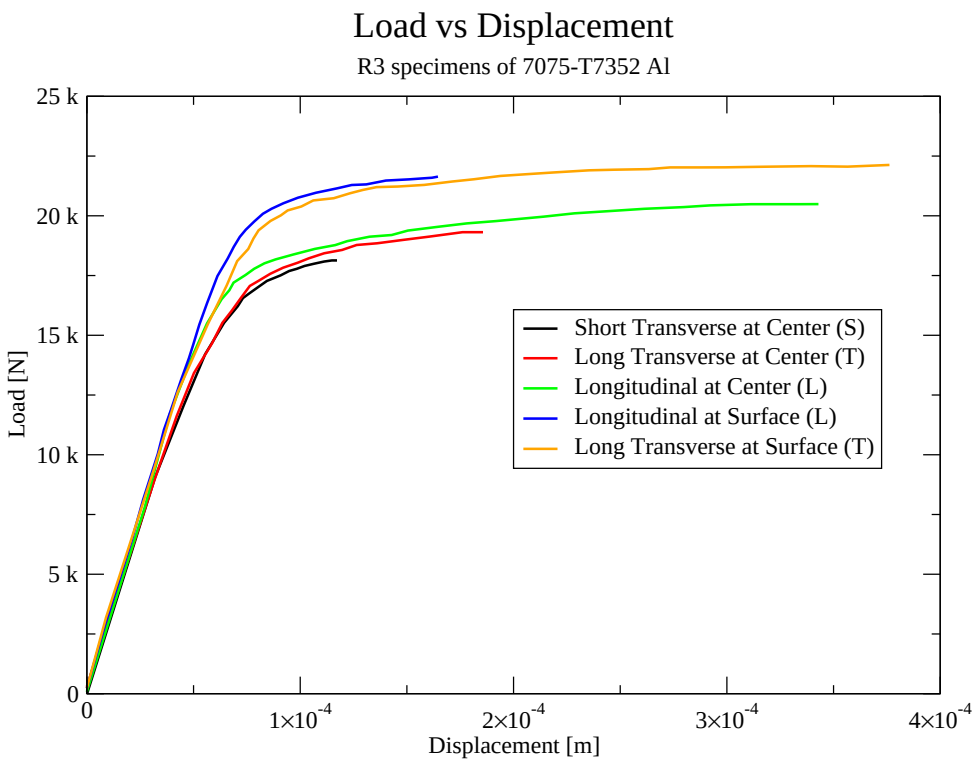

Figure 2.2. Load vs. displacement for R3 specimens of 7075-T7351 aluminum.

posed work will provide useful data for understanding the evolution of damage in aluminum alloys. Figure 2.3 shows a single reconstructed micrograph of a section of a smooth tensile specimen of 7075-T7351 aluminum that had previously been loaded to failure. This particular specimen had been loaded in the short-transverse direction and then one end of the fractured specimen was machined to provide a quarter-round section with lateral dimension on the order of 2.5 mm. The full image on the left shows a cross-section within the 3D fracture zone, capturing the damaged, but non-fractured material just beneath and adjacent to the failure surface. The rolling direction is indicated in this figure by a dashed line. The images show two main features: constituent particles, which are on the order of 5 μm in lateral dimension and appear lighter than the aluminum matrix, and voids, which are the dark regions and are as large as 40 μm. As expected with this type of material, the constituent particles tend to align with the rolling direction in the form of *stringers*. What is more interesting is that the voids are closely associated with these strings of particles. The set of experiments involving in-situ and interrupted testing at various stages of deformation is designed to reveal the detailed nature and evolution of the damage and its relationship to the material microstructure.

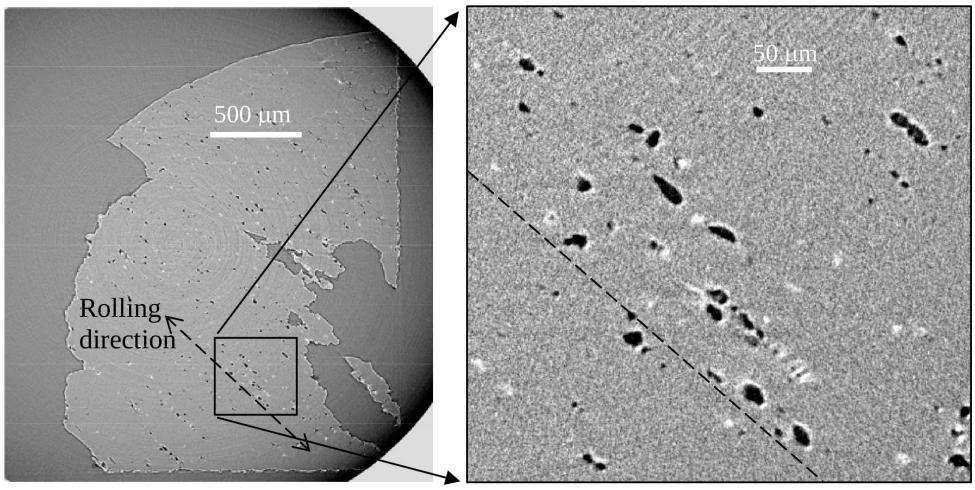

Figure 2.3. Reconstructed cross section near the failure surface of a transverse specimen of 7075-T7351 aluminum.

2.2 The Specimens

We propose to perform a comprehensive set of tests in which the internal damage at the micron-scale will be monitored under different levels of load. Our tests will focus on a single material (7075 aluminum) subject to different modes of deformation that will introduce multiple damage mechanisms. The specimens are designed to allow investigation of the

varying effects of such parameters as loading orientation, stress triaxiality and level of shear. All loading is quasi-static.

We started the experiments with in-situ smooth tensile tests of specimens, followed by a notched specimen. The smooth specimens are cylinders of 1.27mm diameter and 31.75mm length. The notched specimens have a minimum diameter at the root of the notch of 1.5mm, which allows this region to be fully within the image at maximum resolution.

Loading takes place using a loading frame designed at ALS beamline 8.3.2. We performed a series of tomographic observations of the material under increasing load, beginning with the virgin, unloaded specimen and proceeding until failure has occurred. The load is held constant while the X-ray images are collected in order that all images are captured at the same material state. The specimens are fabricated in such a manner that the loading will be oriented along each of the principal material directions and in off-axis orientations (i.e., at 45 degrees to the principal directions) as well.

The corresponding loading programs and indicators of tomographic scans are shown in Figure 2.4. The curves, which correspond to similar specimens, have indicators that show where in the loading program the tomographic scan took place. The actual load levels corresponding to the scanned specimens are shown in Table 2.1, together with a designated name to identify them throughout this report. Where the load level is indicated by a hyphen, the scan was performed on a failed specimen.

Additional tests will involve shear-dominated loading using the Iosipescu or V-rail geometry which uses a traditional uniaxial testing machine to induce a nearly uniform state of shear stress across a section of the specimen [4]. As with the notched tensile tests, specimens will be machined to allow loading both in the principal material directions and in the off-axis directions.

For each specimen we estimate that approximately eight tomograms will be required to monitor the evolution of damage during the deformation. The first will characterize the virgin material, then tomograms will be taken at approximately five load levels prior to specimen failure. After failure, two additional tomograms will be taken one associated with material near each of the failure surfaces. We requested a total of 72 shifts over the two year span of the experimental work to complete all of the desired measurements.

The data collected through these observations will play a key role in the ongoing modeling of anisotropic damage in structural materials of our team, of which the quantification of the debonding of inclusions that concerns this report is part. To this end, we use the high-performance visualization infrastructure at Sandia to construct virtual 3D models and thus visualize, explore and mine the data provided by the experiments performed at the ALS.

We focus on the nucleation of voids and their association with the microstructure of the material with loading. Since for each specimen, we have data from the unloaded state to the failed state, we should be able to track individual microstructural features throughout the damage evolution process. The experimental team consists of Prof. George C. Johnson, Department of Mechanical Engineering, University of California at Berkeley and a group

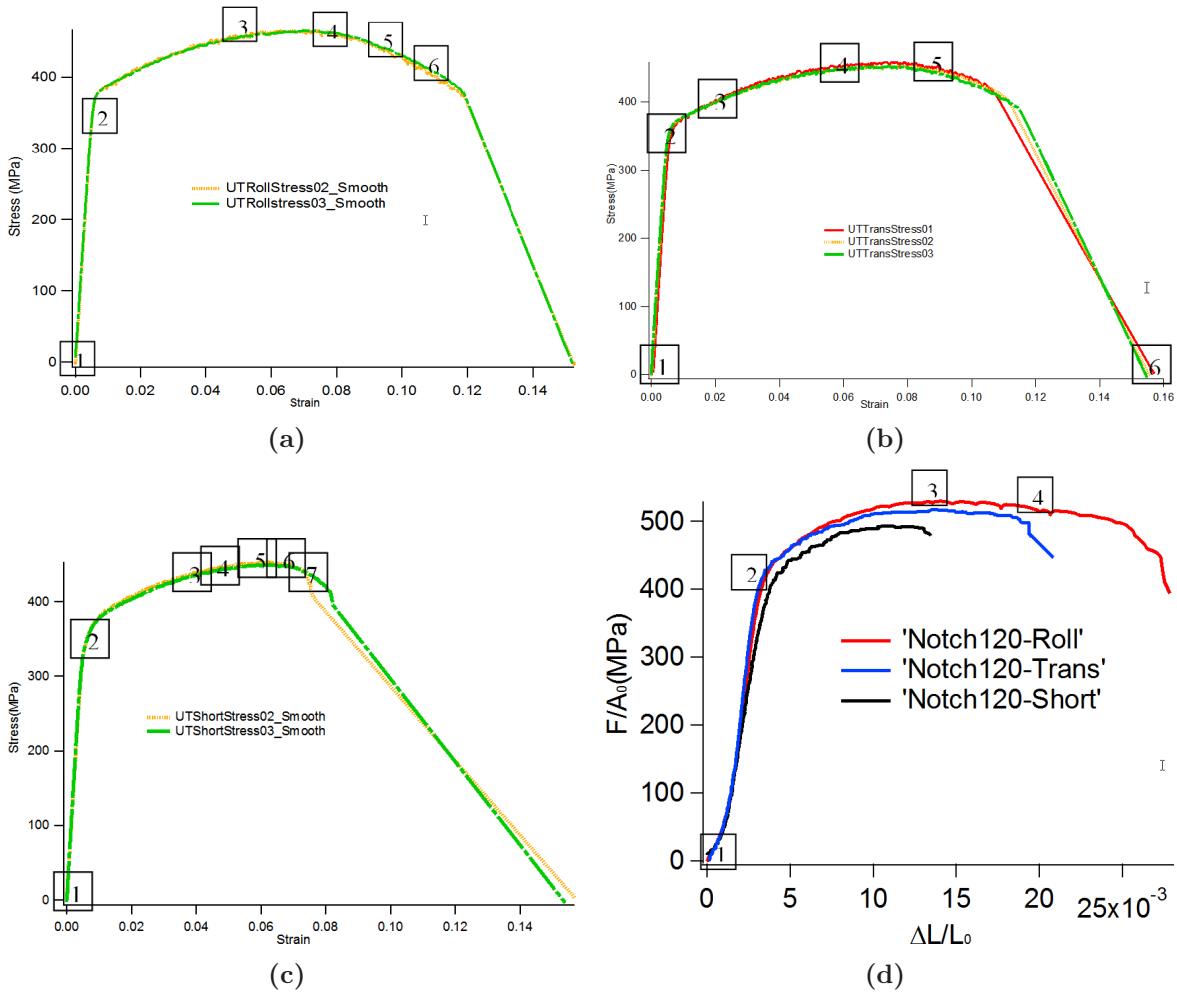

Figure 2.4. Loading programs and directions with scan indicators: (a) Smooth specimen, longitudinal (L); (b) Smooth specimen, long transverse (T); (c) Smooth specimen, short transverse (S); (d) Notched specimen, longitudinal (L).

(a) Smooth L

Scan number	Stress [MPa]	Designation
1	37.75	SL1
2	381.25	SL2
3	452.97	SL3
4	456.75	SL4
5	430.32	SL5
6	407.68	SL6
7	-	SL7

(b) Smooth T

Scan number	Stress [MPa]	Designation
1	38.26	ST1
2	362.45	ST2
3	406.48	ST3
4	473.12	ST4
5	452.55	ST5
6	-	ST6

(c) Smooth S

Scan number	Stress [MPa]	Designation
1	38.62	SS1
2	390.02	SS2
3	451.81	SS3
4	455.67	SS4
5	463.39	SS5
6	447.94	SS6
7	428.64	SS7

(d) Notched L

Scan number	Stress [MPa]	Designation
1	35.09	NL1
2	477.23	NL2
3	533.38	NL3
4	529.87	NL4

Table 2.1. Scans and load levels.

of researchers from Sandia National Laboratories in Livermore, California: James Foulk, Huiqing (Helena) Jin, Wei-Yang Lu and Alejandro Mota. This team brings a broad range of expertise in experimental micro- and nano-mechanics, constitutive modeling and computational analysis.

Chapter 3

Tomography and Reconstruction

The process of acquiring tomographic data can be divided in two phases: scan and reconstruction. During the scan process the specimen is subjected to the X-ray beam, and a camera captures the projected image. The specimen is rotated and the process repeated to obtain projections from different angles. These projections are difficult to interpret, thus further processing is required. It is possible to build a 3D representation of the original specimen using these projections by a process known as reconstruction. We briefly discuss the parameters used in the scans and concentrate in the reconstruction, which is a sensitive procedure.

3.1 Tomographic Scan

Data obtained from SRCT consist of gray-scale 2D images which show attenuation to soft X-rays (5-60keV, 0.248-0.021nm). This attenuation can be correlated to the mass density of the material, with bright areas being zones of higher density (inclusions) than dark areas (voids). These images are processed further by reconstruction to obtain full 3D representations that reveal the internal structure of the material.

The resolution of SRCT data is 900nm, which allows elucidation of the mechanisms governing void growth and coalescence. This resolution is not fine enough, however, for nucleation. We propose the use of statistics and image processing techniques to obtain sub-resolution scale information from these data, and thus determine where in the specimen and when during the loading program nucleation occurs and the mechanisms that lead to it.

3.2 The Reconstruction Process

The operation which is being performed on the scanned data is known as the Radon transform [7, 8]. It provides a way to relate an n-dimensional function to its $(n-1)$-dimensional projections (sinograms). For X-ray computed tomography, the analogy between the Radon transform and our data is adequate under the assumption that the following do not introduce significant distortions:: the photon beam has a finite size and is not completely collimated.

Assume that the object can be sampled with infinite resolution. In other words, the beam travels in a straight line and is infinitely thin along its whole length. As a result, any scattering from the object is a source of model error. In order for tomography to work in a straightforward way, the beam must interact with the object only through absorption. Photons either pass through a section of the object without interaction or they are absorbed. Note that re-emission at a different energy is acceptable as long as these photons cannot be detected by the measurement equipment. It is possible to account for scattering within the volume, but this is not standard X-ray tomography. Single scattering within the volume results in linear blurring of the object and can be incorporated into a Radon transform framework. Multiple scattering (the photon interacts more than once before exiting the viewing volume) is a non-linear effect. For this reason, objects should interact with the beam only weakly, as defined by the first Born approximation [7, 8].

Since we are attempting to reconstruct a 3D volume and at the moment we are ignoring sampling effects, the data that are collected are 2D projections (sinograms) of a 3D object. In each data set, bright spots exist where the object was less dense, and dark spots occur where the object is dense as a result of more absorption. Brute force inversion of the Radon transform occurs in two steps: 1) Compute the adjoint of each of the data sets. This is known as back-projection. The data is smeared back across the viewing volume so that the reconstructed quantity (absorption coefficient) is assumed to be constant over a line passing through the volume to the detector. This is the same line that the X-ray took to the detector. 2) Repeat step 1 with all of the data sets and perform a sum.

The *linear attenuation coefficient* $\mu_{\bar{e}}^S$ of the object S at energy $\bar{e}$ is defined as

$$\mu_{\bar{e}}^S := -\log(\rho), \tag{3.1}$$

in which ρ is the probability that a photon of energy $\bar{e}$ will *not* be absorbed or scattered in a unit-thickness slab of the object S on a line orthogonal to the slab. The *relative* linear attenuation coefficient is defined as

$$\mu_{\bar{e}} := \mu_{\bar{e}}^S - \mu_{\bar{e}}^0, \tag{3.2}$$

in which $\mu_{\bar{e}}^0$ is a reference linear attenuation coefficient, that of air on our case. Roughly speaking, the *CT number* that is obtained for each voxel after reconstruction is proportional to its average relative attenuation coefficient. Note that the relative attenuation coefficient leads to dark regions where the material is less dense and bright regions where the material is more dense, in contrast to the 2D projections (sinograms).

Assume that the reconstruction process takes place in slices perpendicular to a vertical axis. Then let L be the straight line that is the path of all the X-ray photons for a particular source-detector pair and let m be the corresponding monochromatic ray sum. Then this sum can be approximated by

$$m \approx \int_0^D \mu_{\bar{e}}(x, y)\, dz, \tag{3.3}$$

in which z is the distance to the point along the line L, x and y are the coordinates of a point in a given slice, and the integration limits denote the nearest and farthest surfaces of

the object along the line L, respectively. Now let l denote the distance of line L to the origin, and let θ be the angle between x and L. The Radon transform is [7, 8]

$$\mu_{\bar{e}}(x,y) = -\frac{1}{2\pi^2} \lim_{\varepsilon \to 0} \int_{\varepsilon}^{\infty} \frac{1}{q} \int_0^{2\pi} \frac{\partial m}{\partial l}(x\cos\theta + y\sin\theta, \theta)\, d\theta\, dq. \tag{3.4}$$

The implication of this transform is that the distribution of the relative linear attenuation in an infinitely thin slice is uniquely determined by the set of *all* its line integrals. There are some important difficulties, however, in applying this transform to computed tomography, some of which we address in the next section.

3.3 Reconstruction from Sampled Data

It is known that any insufficiency in the data leads to aliasing (artifacts) in the reconstructed object [7, 8]. Perfect Radon reconstruction is only possible if the projections are known with infinite precision at all points. This is because any finite sized object cannot have limited spatial frequency content; therefore any frequency content beyond the Shannon-Nyquist limit will be aliased into lower frequencies. This has the effect of adding a null space to the Radon operator. Thus, a priori information must be introduced to resolve the ambiguity.

An effective but simple assumption is that the object which is desired is the object with the minimum energy. More sophisticated reconstruction methods may allow for edges and other image features to be penalized less severely.

The null space has other implications with respect to noise. This noise could arise from the photon counting process or the quantization of the detector voltage. Below a certain signal to noise ratio it is desirable to limit the contribution of the noisy data to the reconstructed object. The most popular method is known as Tikhonov regularization, which allows fidelity to the data and the fidelity to the minimum energy solution to be traded off in a linear fashion with respect to the signal to noise ratio. Using regularization ensures that the reconstructed absorption coefficient does not go to infinity when there is low signal to noise ratio.

There are a number of reconstruction algorithms. The most efficient of these is based upon the Fourier slice Theorem and is attributed to Delaney and Bresler [5]. The Fourier slice theorem says that the Fourier transform of a projection yields a slice of the Fourier transform of the object in a direction orthogonal to the viewing direction (in Fourier space). The last part is, in some sense, not all that important because it simply results in a rotation of the object. If the object is highly symmetric, however, this could lead to significant aliasing. Delaney and Bresler [5] contribution was to realize that there is a significant amount of redundancy in the Fourier transform computations. As a result, it is possible to reconstruct a 2D slice in $O(n\log(n))$ operations as opposed to $O(n^2\log(n))$ for the basic Fourier reconstruction algorithm. Note that the Fourier transform is an $O(n\log(n))$ algorithm, where n is the number of pixels. One can trade off reconstruction accuracy for increased sampling and computational requirements.

In summary:

1. The Radon transform (3.4) determines the reconstruction from the set of *all* line integrals. In computed tomography there exist only a finite set of measurements.

2. The measurements are assumed to contain information used to estimate the line integrals. Inaccuracies in these estimates due to the finite size of the X-ray beam, scatter, photon statistics, detector inaccuracies and so forth could severely affect the result of the Radon transform.

3. It is not trivial to obtain and efficient and accurate algorithm for the implementation of the Radon transform. Much research has been performed in the development of algorithms that yield acceptable reconstructions in a timely manner and that work well with limited and inaccurate data [5, 7, 8].

For our scans, we were limited to the reconstruction software available at the Advanced Light Source. The software package is called Octopus [2].

Chapter 4

Quantitative Analysis of Tomography Data

Synchrotron-radiation computed tomography (SRCT) is a technique that provides information about the internal structure of a material by probing it with soft X-rays. The attenuation of the X-rays is directly correlated to the mass density of the material, thus providing information about the internal structure of a specimen. Data obtained from the SRCT scanner are in the form of a series of 2D images, each of which show the internal structure of the specimen in a slice that has a thickness equal to the resolution of the scanner, which is 900nm for the Advanced Light Source (ALS). A full 3D scan of the specimen is built by combining the series of 2D images into a stack with ImageJ, an image-processing software from the National Institutes of Health [1]. The data thus produced ranges from 5 GB to 25 GB per scan. Each data set is rendered using ParaView [3] on high capacity computing clusters at Sandia, due to the size of the data sets and the high amount of computing power and memory required to process them.

4.1 Distribution of Attenuation in Scans

Each voxel in the 3D image has a 16-bit integer associated with it, its *CT number*, which is proportional to its average relative attenuation (3.2) to soft X-rays, and which henceforth will be referred to as attenuation. The images are further processed by building a histogram of these integers. A typical view of the reconstructed images as obtained from Octopus [2] is shown in Figure 4.1

Another typical reconstructed image, this time from scan NL4 is shown in Figure 4.2, where the dark areas indicate voids and the bright areas hard particles. The pixel resolution is 900nm.

In order to be able to distinguish between the aluminum matrix, hard particles, and voids in the images we need to determine which values of their corresponding attenuation distinguish them. First start by constructing histograms of attenuation values of regions that are visually devoid of bright or dark zones. The corresponding histograms of attenuation values are normalized so that their mean is equal to zero and their standard deviation equal to

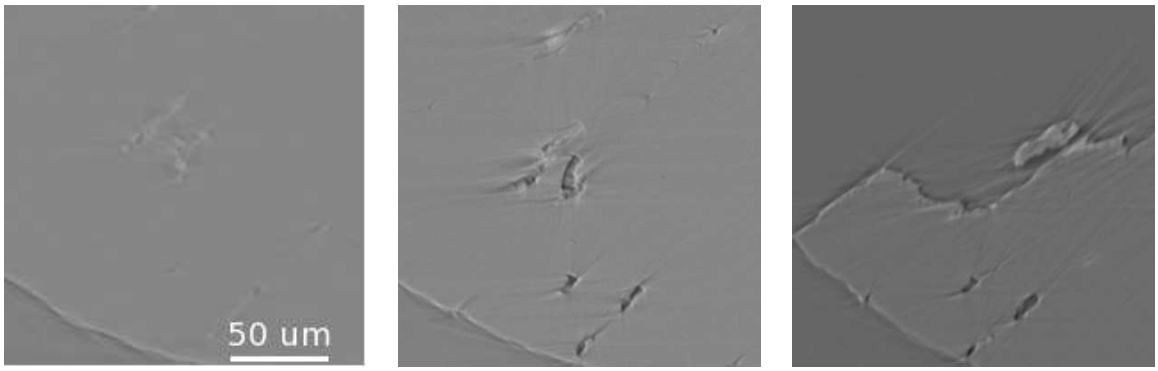

(a) (b) (c)

Figure 4.1. Typical section of reconstructed images for smooth transverse (T) specimen near the center: (a) ST1, near intact; (b) ST5, void growth; (c) ST6, coalescence and rupture.

one. Figure 4.3 shows the results. It is evident from the figure that the resulting distributions are close to a normal probability distribution.

By contrast, the attenuation distribution of a region in the scan that is outside the specimen is essentially a Dirac δ, as shown in Figure 4.4. This indicates that the attenuation distribution in the matrix is a feature of the matrix and not the scan or reconstruction processes.

Low (voids) and high (inclusions) density regions can then be extracted by filtering from the image voxels that deviate from the normal distribution. A typical histogram with the distribution of the attenuation values for a scan is shown in Figure 4.5.

The histogram was produced by taking all the slices in the reconstruction of scan ST1 and extracting a rectangular parallelepiped (the size in pixels of which is shown in the heading of the plots) that avoids the boundaries of the specimen. The boundary is not included as it contains a high concentration of voxels with both low and high attenuation values, which would bias the statistics. This effect does not seem to be a genuine structural feature of the specimen but rather an artifact of either the scan or reconstruction.

Note that the histogram of Figure 4.5 still shows a rather smooth distribution of the attenuation values but one that deviates significantly from a normal distribution. For comparison, a normal distribution with the same mean and standard deviation is shown as a black line in the figure. A distribution with a more pronounced peak than the normal distribution has high kurtosis, which means that there are significant contributions to the standard deviation from outliers. For this particular scan the statistics are shown in Table 4.1.

Given the very large size of the data sets (almost 2 billion voxels for this set alone), the

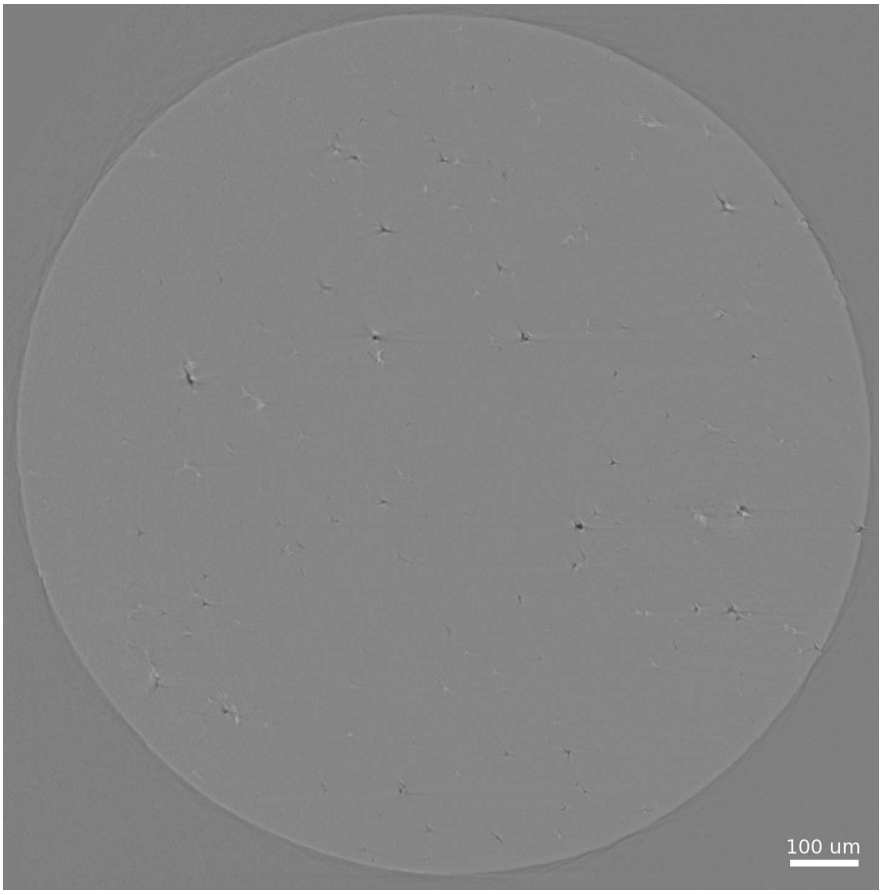

Figure 4.2. NL4 scan near the center of the specimen. Dark areas are voids and bright areas are particles. Diameter of specimen is 1.27mm

Number of voxels (N):	1904894496
Mean (μ):	34819.6
Standard deviation (σ):	698.2
Skewness (γ):	-0.6
Kurtosis (κ):	56.0

Table 4.1. Statistics for scan ST1.

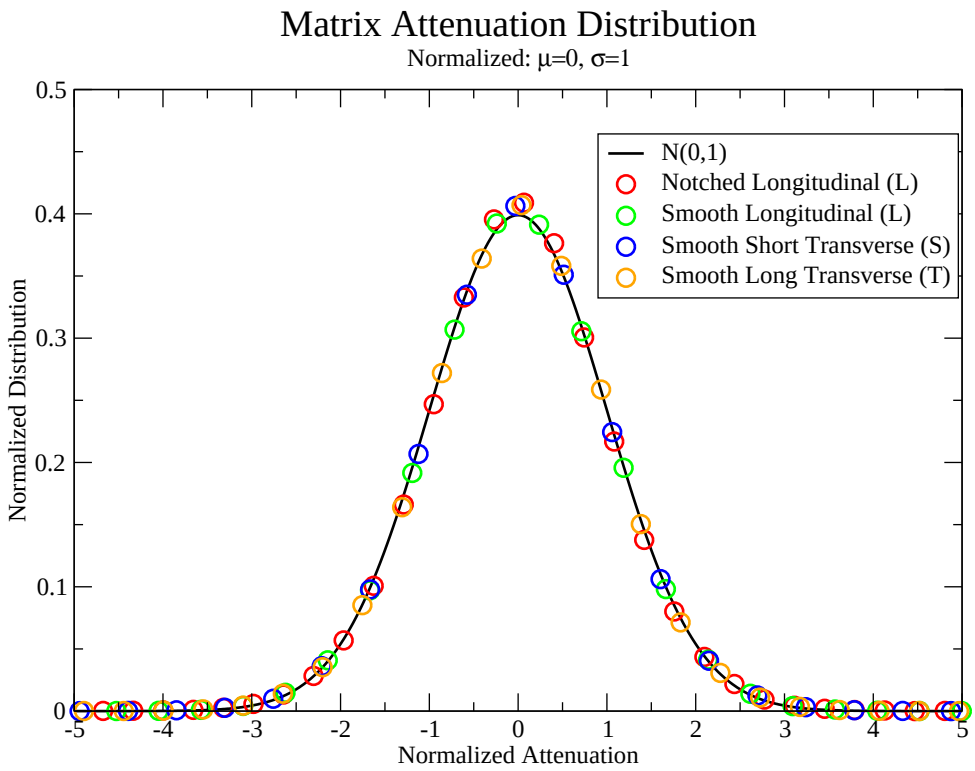

Figure 4.3. Normalized distribution of aluminum matrix attenuation values ($\mu = 0$, $\sigma = 1$) compared with the normal distribution N(0,1).

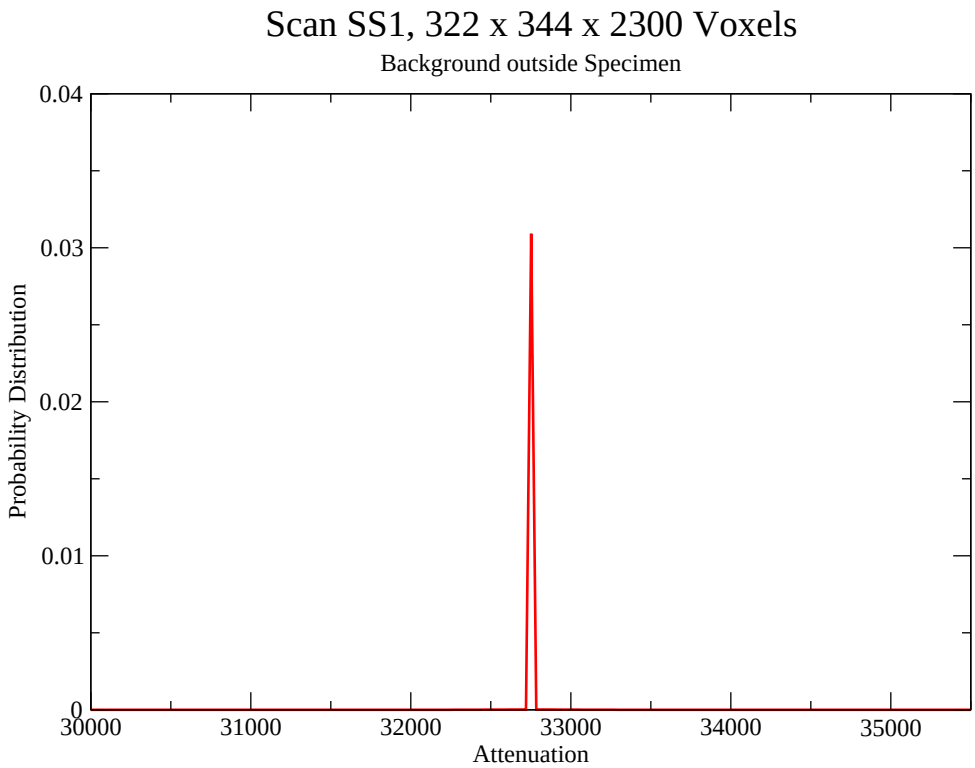

Figure 4.4. Distribution of attenuation values outside specimen for scan SS1.

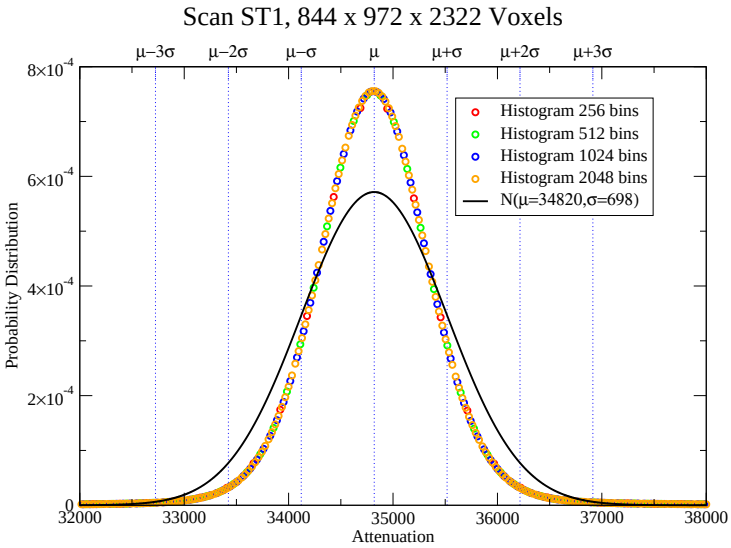

(a)

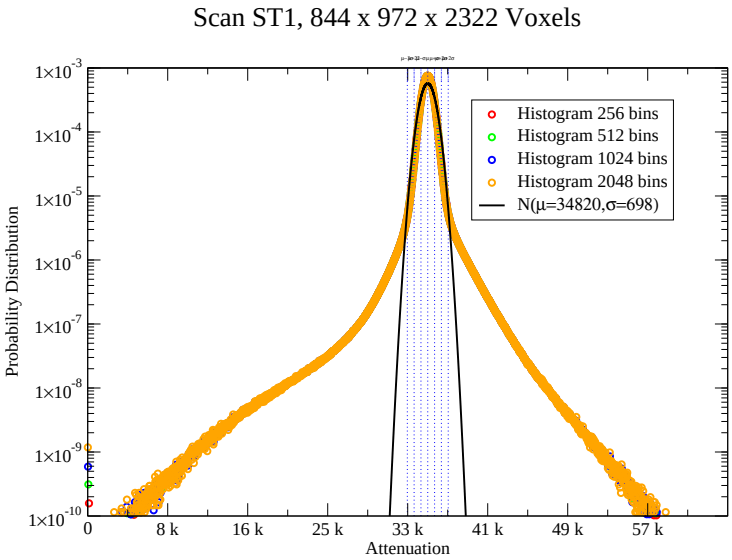

(b)

Figure 4.5. Histogram of attenuation values for scan ST1: (a) linear-linear scale; (b) linear-log scale.

statistics are computed by means of moments about zero that are transformed into moments about the mean. In this manner, the statistics are computed in a single pass as follows

$$\mu_k := \frac{1}{N}\sum_{i=1}^{N} x_i^k, \quad k \in [1, \ldots, 4], \tag{4.1}$$

$$\bar{\mu}_3 := \mu_3 - 3\mu_1\mu_2 + 2\mu_1^3, \tag{4.2}$$

$$\bar{\mu}_4 := \mu_4 - 4\mu_1\mu_3 + 6\mu_1^2\mu_2 - 3\mu_1^4, \tag{4.3}$$

$$\mu := \mu_1, \tag{4.4}$$

$$\sigma := \sqrt{\mu_2 - \mu_1^2}, \tag{4.5}$$

$$\gamma := \frac{\bar{\mu}_3}{\sigma^3}, \tag{4.6}$$

$$\kappa := \frac{\bar{\mu}_4}{\sigma^4} - 3, \tag{4.7}$$

in which N is the number of voxels in a given set, x_i the attenuation value for voxel i, μ is the mean, σ is the standard deviation, γ is the skewness, and κ is the excess kurtosis, defined in a way that both the skewness and kurtosis of the normal distribution are zero.

The statistics for all the scans (except SL7, for which the reconstruction showed heavy artifacts, rendering it useless) are summarized in Table 4.2.

Given that the attenuation distribution for all the scans is similar to the normal distribution, we provide an interpretation for the skewness and kurtosis in terms of a comparison with their corresponding values for the normal distribution, which are zero.

Positive skewness means a distribution tilted toward $-\infty$ and negative skewness means a distribution tilted toward $+\infty$, both with respect to a distribution with zero skewness. Note that all scans have relatively low negative skewness, which means that their distributions of attenuation are highly symmetric, as it is evident from the example in Figure 4.5.

Kurtosis is a measure of the concentration of values around the mean. A leptokurtic distribution (high kurtosis) has a high central peak and many outliers as compared with the normal distribution. A platykurtic distribution (low kurtosis) has a flattened central peak and few outliers as compared to the normal distribution. Note that the attenuation distributions for all scans are highly leptokurtic, which means that they contain a significant amount of outliers and a high peak at the center, as it is evident from Figure 4.5.

4.2 Separation of Voids and Particles

The distribution of attenuation values in the aluminum matrix follows closely that of the normal distribution, as seen in Figure 4.3; while the background is highly monochromatic, as shown in Figure 4.4. These two observations indicate that the normal distribution of the matrix attenuation values is a feature of the specimen.

Scan	Number of Voxels N	Mean μ	Std Dev σ	Skewness γ	Kurtosis κ
NL1	1493515944	38290.6	712.0	-0.6	32.4
NL2	1518934032	34458.7	645.7	-0.5	30.3
NL3	1401099000	34439.6	654.5	-1.0	38.1
NL4	1365235320	34459.5	681.5	-1.4	46.7
SL1	2301320960	30978.9	628.4	-0.7	60.8
SL2	2131860605	34849.6	706.7	-0.5	42.1
SL3	1974380079	34432.9	588.5	-0.7	44.8
SL4	1726160744	34428.9	639.5	-0.7	30.2
SL5	1542430692	34435.3	693.5	-2.6	83.1
SL6	1466857008	34443.4	747.9	-3.5	96.1
SS1	2084499200	34222.2	533.0	-0.8	56.0
SS2	2048435200	34383.3	601.5	-0.8	54.2
SS3	1954356000	34385.1	633.9	-1.4	59.9
SS4	1878272000	34386.9	679.2	-2.3	77.6
SS5	1871206400	34388.7	696.0	-2.5	81.5
SS6	1846365204	34389.5	744.4	-3.1	90.6
SS7	364860840	34365.3	627.1	-0.3	8.1
ST1	1904894496	34819.6	698.2	-0.6	56.0
ST2	1895833544	34408.7	556.6	-1.5	91.3
ST3	1891507845	34411.9	556.6	-1.1	67.8
ST4	1792388864	34414.9	575.6	-1.2	66.1
ST5	1557048744	34417.6	748.2	-3.3	97.4
ST6	766397352	27870.9	703.0	-4.6	118.9

Table 4.2. Statistics for all scans.

On the other hand, the high values of kurtosis observed in Table 4.2 for all scans indicate a significant presence of outliers that are located toward the tails of the distribution. This is evident in the semi-logarithmic plot of Figure 4.5.

These observations suggest that in order to find the distribution of outliers contained in the full histogram of a scan, such as the one in Figure 4.5, one would need first to identify the normal distribution associated with the attenuation values of its matrix. Provided that this identification can be performed, the distribution of outliers would be given by the difference between the full distribution and the matrix normal distribution.

The identification of the normal distribution associated with the matrix was performed using two methods: 1) A least-squares fit using the central part of the histogram that has no obvious outliers (from $\mu-\sigma$ to $\mu+\sigma$), and 2) The random sample and consensus approach or RANSAC [6], which finds a model from data that contains a significant amount of outliers. The theory behind the RANSAC method is not addressed here; we defer to Fischler and Bolles [6] who first introduced this technique.

The results of using both the least-squares and RANSAC approaches are shown in Figure 4.6. It shows the normalized scan histogram (circles), a normal distribution with the same mean and standard deviation as the full distribution (black), the best-fitting normal distribution found by RANSAC (blue), a normal distribution that was fitted by least-squares to the central part (red), and the difference between the full distribution and the least-squares fit (green).

The results shown in Figure 4.6 are typical in the sense that, in our computations, the least-squares approach consistently produced better results than the RANSAC approach. Although the theory behind the RANSAC method is sound and robust, it is known that in order to find the model that best fits the data with a high probability, the RANSAC algorithm may require a large number of iterations. We found that the computational expense associated with the RANSAC approach was not justified, especially considering that in this case the location of outliers is known beforehand, and therefore one can quickly produce a good fit by using least squares.

The central part of the outlier distribution computed in this manner sometimes yields small negative values. These values are unrealistic and are associated with fits that have larger distribution values than the original curve. These negative values can be ignored, as we are interested in outliers at the tails. With this in mind, we now proceed to define the criterion that separates voids and particles from the aluminum matrix. The green curve in Figure 4.6 indicates the difference between the full attenuation distribution and the normal distribution associated with the matrix. Thus, it also indicates the attenuation distribution of outliers. Note that the full histogram is the only true probability density function (PDF)

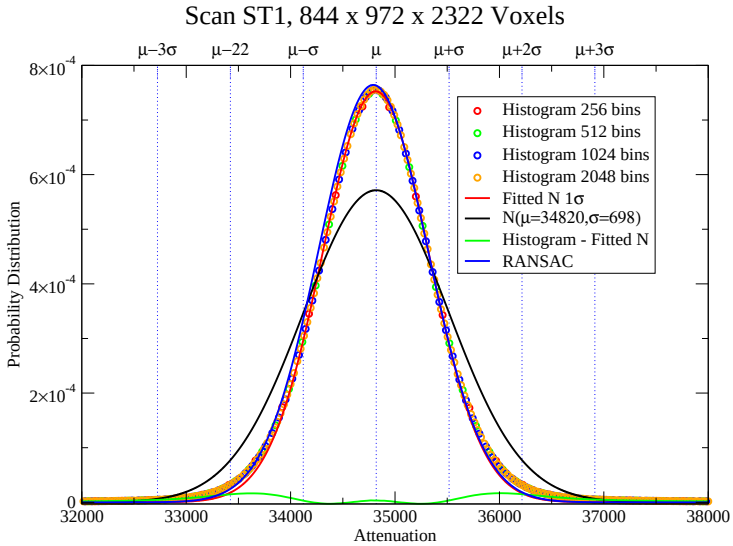

(a)

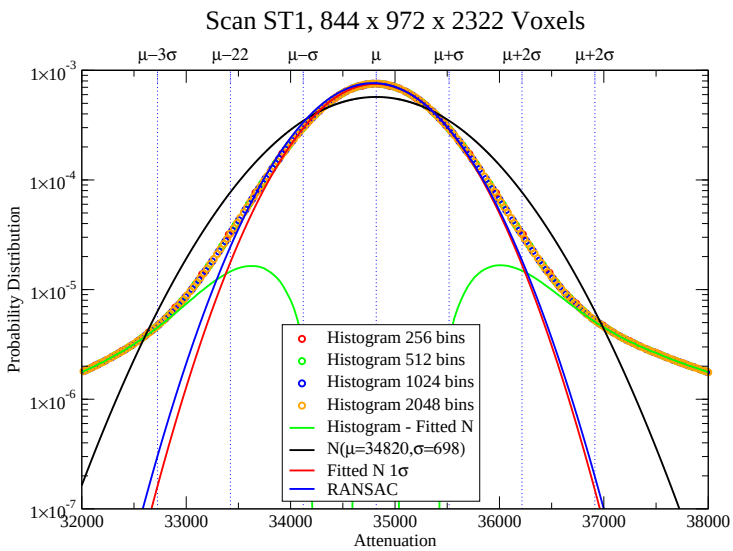

(b)

Figure 4.6. Identification of matrix normal distribution for scan ST1. Black, normal with μ and σ. Red, least-squares fit. Blue, RANSAC fit. Green, outlier distribution. (a) linear-linear scale; (b) linear-log scale.

involved here, in the sense that

$$P[a \leq X \leq b] = \int_a^b f(x)\,dx, \tag{4.8}$$

$$\int_{-\infty}^{+\infty} f(x)\,dx = 1, \tag{4.9}$$

$$f(x) = g(x) + h(x), \tag{4.10}$$

in which X is a random attenuation value, $f(x)$ represent the histogram (taken as a continuous function), x is the attenuation (taken as continuous as well), and $g(x)$ and $h(x)$ are functions representing the matrix and outlier attenuation distributions, respectively. It follows from these definitions that, given $p \in [0, 1]$, the attenuation value x with probability of being an outlier p and probability of being in the matrix $1 - p$ is given by solutions of

$$p\,h(x) = (1 - p)\,g(x), \tag{4.11}$$

if such solutions exist. As an example, assume that $p = \frac{1}{2}$, which means finding attenuation values for which it is equally likely that they are part of the matrix or outliers. The criterion (4.11) is reduced to finding solutions for $h(x) = g(x)$. In terms of Figure 4.6 this requires finding points where the green and red curves intersect, if any such points exist. From the figure, in particular in the semi-logarithmic plot, it is clear that two such points exist, one at each tail of the distribution. Thus, there are two attenuation values for which it is equally likely that they correspond to matrix or outliers: one for voids for the left tail and one for particles for the right tail.

Solving (4.11) for a given p does not pose significant computational challenges, as the histograms are represented as pairs of values (attenuation, distribution). Therefore finding solutions is relatively simple by using interpolation between points.

The results of applying criterion (4.11) to all the scans with $p = 0.95$ are shown in Table 4.3. The selected value of $p = 0.95$ gives reasonable assurance, with 0.95 probability, that each limit (α for voids and β for particles) separate outliers from the matrix.

A visualization of the criterion applied to scan ST1 is shown in Figure 4.7, which shows the central part of the specimen looking down the loading axis. The high density of both voids and particles is due to the fact that the entire length of the specimen is represented in the figure. The rolling direction in the specimen appears to be oriented at about 135 degrees.

4.3 Extraction of Under-Resolved Information

The approach defined in (4.11) is more than adequate to reveal the structure of inclusions and voids in the material, and provides the means to establish the mechanisms that lead to the formation of void chains, void sheets, and eventually fracture surfaces. The resolution of the images, however, is insufficient to elucidate the mechanisms that lead to nucleation of the

Scan	Scan Mean μ	Scan Std Dev σ	Fit Mean $\bar{\mu}$	Fit Std Dev $\bar{\sigma}$	Void Threshold $\alpha(0.95)$	Particle Threshold $\beta(0.95)$
NL1	38290.6	712.0	38287.9	596.8	35800	40744
NL2	34458.7	645.7	34456.4	538.9	32217	36662
NL3	34439.6	654.5	34437.8	533.3	32223	36610
NL4	34459.5	681.5	34458.0	541.8	32215	36653
SL1	30978.9	628.4	30975.5	477.8	29040	32900
SL2	34849.6	706.7	34845.2	546.0	32646	37024
SL3	34432.9	588.5	34430.6	468.4	32514	36327
SL4	34428.9	639.5	34428.2	504.8	32389	36445
SL5	34435.3	693.5	34436.2	468.0	32572	36276
SL6	34443.4	747.9	34444.1	477.7	32539	36319
SS1	34222.2	533.1	34219.9	423.5	32472	35954
SS2	34383.3	601.5	34380.9	473.2	32434	36313
SS3	34385.1	633.9	34382.4	479.2	32414	36320
SS4	34386.9	679.2	34384.6	485.2	32404	36328
SS5	34388.7	696.0	34386.3	490.0	32389	36343
SS6	34389.5	744.4	34388.9	500.3	32356	36377
SS7	34365.3	627.1	34370.5	533.8	32232	36525
ST1	34819.6	698.2	34814.6	523.4	32703	36903
ST2	34408.7	556.5	34404.2	410.6	32729	36063
ST3	34411.9	556.6	34407.4	413.6	32735	36061
ST4	34414.9	575.6	34410.7	419.5	32724	36076
ST5	34417.6	748.2	34418.8	456.8	32606	36201
ST6	27870.9	703.0	27879.5	388.0	26348	29415

Table 4.3. Normal fits and void and particle thresholds for $p = 0.95$.

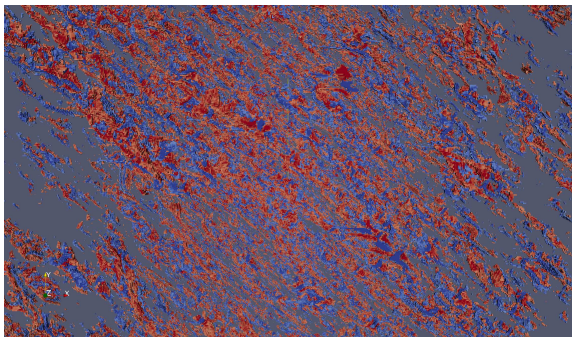

(a)

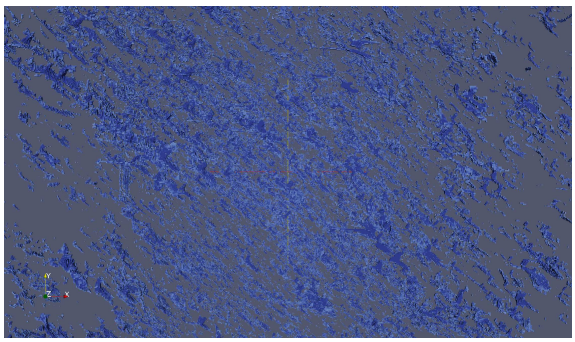

(b)

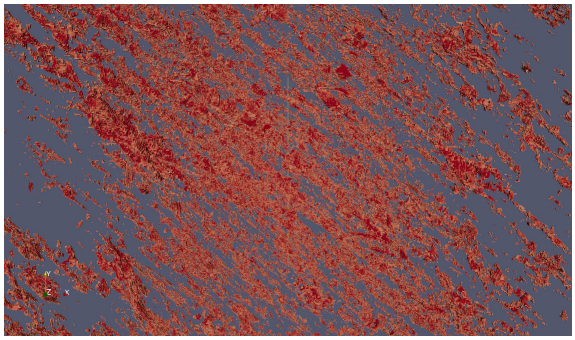

(c)

Figure 4.7. Scan ST1 after applying separation criterion (4.11) with $p = 0.95$. Voxel size = 900nm (a) all outliers; (b) voids; (c) particles.

voids, namely, the initial formation of a void from the debonding of the interface between an inclusion and the metallic matrix, or the propagation and growth of a void from an already debonded interface that existed in the undamaged material.

Casual observation of the images reveals that in the damaged state there exist regions of lower-than-average density around inclusions that are relatively far away from the most damaged regions. This seems to indicate that there is a process of debonding and void nucleation in progress around these inclusions. Nevertheless, the resolution of the images provided by SRCT is 900nm per voxel, which is not fine enough to determine the evolution of the nucleation process with confidence.

The full 3D image for each scan can be filtered to contain only voxels that have an attenuation value below the threshold that defines voids as given in Table 4.3. The image is then transformed to binary by assigning a value of 1 to present voxels and 0 to absent voxels. The image contains now information about voids only, which can be analyzed using state-of-the-art tools of computational homology to determine the evolution of debonding [9, 10].

In particular, the computation of the Betti numbers is most relevant to the determination of whether interfaces are debonded or not. In summary, for a three-dimensional topological space X, only the first three Betti numbers B_i are relevant (the rest are zero): the first number B_1 is the number of connected components in the space, B_2 is the numbers of tunnels, and B_3 is the number of isolated voids. It can be seen that the number of connected components is directly related to fully debonded inclusions, the second to partially debonded inclusions and the third to fully formed voids.

4.4 Error in Reconstruction

We start by quantifying the volume fraction of voids and particles as follows. Once the attenuation thresholds for voids and particles have been defined, these fractions follow immediately by simple voxel counting. The results of these computations are shown in Table 4.4.

The nature of the volume fractions with loading can be better appreciated in Figure 4.8. The significant change of particle volume fraction with loading for all specimens is completely unexpected. This is not something that can be realistically attributable to the kinetics of the loading and deformation, and one can only conclude that there is a significant source of error either in the scanning or reconstruction processes.

As supporting evidence that the reconstruction is the source of the error, Figure 4.9 shows sections of reconstructed slices for different scans. In each of the sections, artifacts in the form of wings, streaks or both propagate from voids and particles. These artifacts enter the statistics as spurious outliers, compromising the reconstructions and rendering them inadequate for quantitative analysis, as demonstrated in Table 4.4 and Figure 4.8.

Scan	Void Volume Fraction $f \times 10^{-3}$	Particle Volume Fraction $h \times 10^{-3}$
NL1	2.06	3.04
NL2	2.17	3.25
NL3	2.57	3.54
NL4	2.91	3.92
SL1	3.88	5.49
SL2	3.99	5.66
SL3	3.13	4.45
SL4	4.02	4.85
SL5	6.22	7.47
SL6	6.62	8.13
SS1	2.74	4.07
SS2	2.94	4.29
SS3	3.39	5.49
SS4	4.13	5.94
SS5	4.34	6.21
SS6	4.96	6.87
SS7	4.12	2.55
ST1	4.36	5.98
ST2	3.77	5.54
ST3	4.22	5.97
ST4	4.73	6.43
ST5	7.55	9.33
ST6	9.27	9.22

Table 4.4. Void and particle volume fractions.

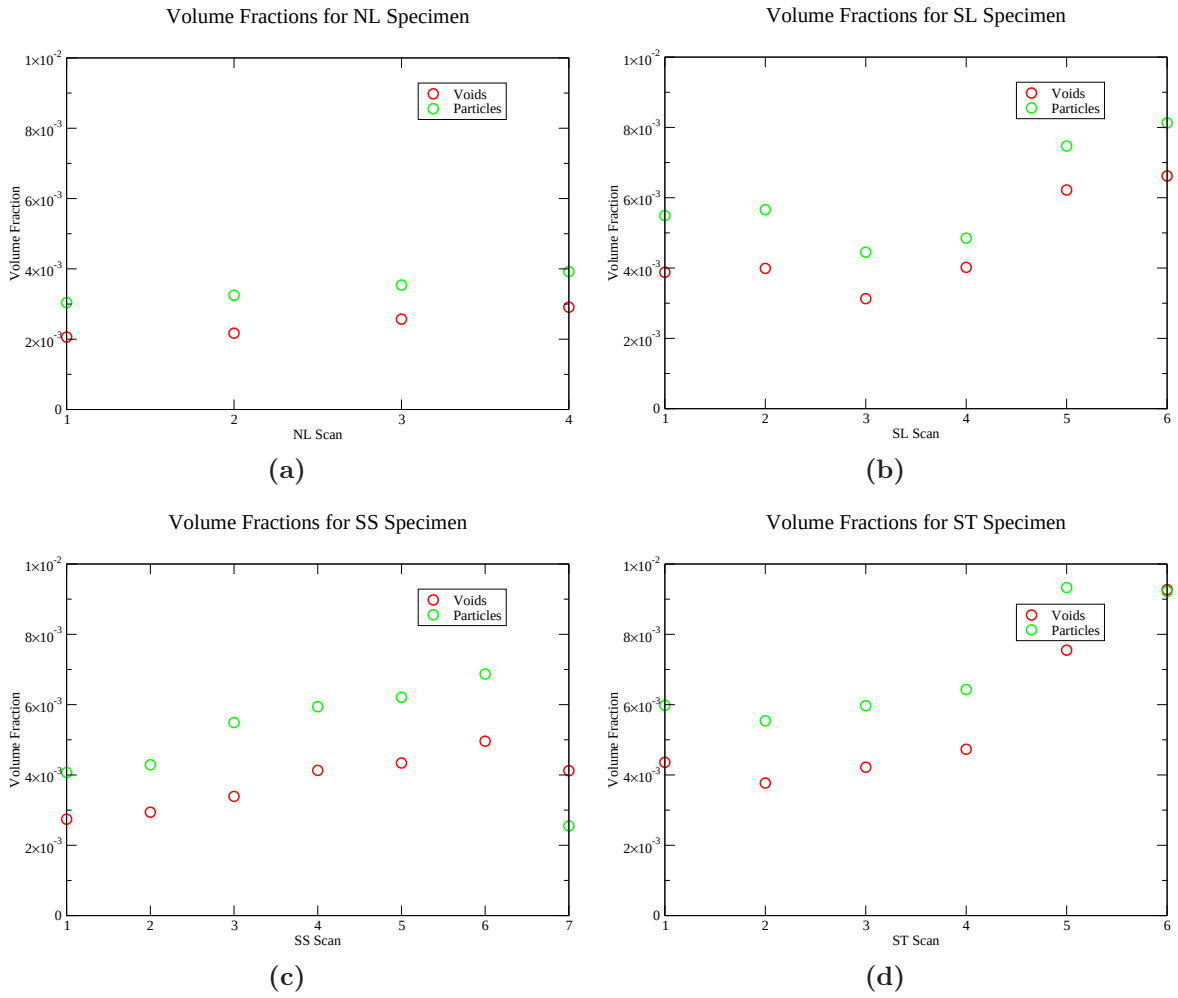

Figure 4.8. Evolution of void and particle volume fractions with loading: (a) NL Specimen; (b) SL Specimen; (c) SS Specimen; (d) ST Specimen.

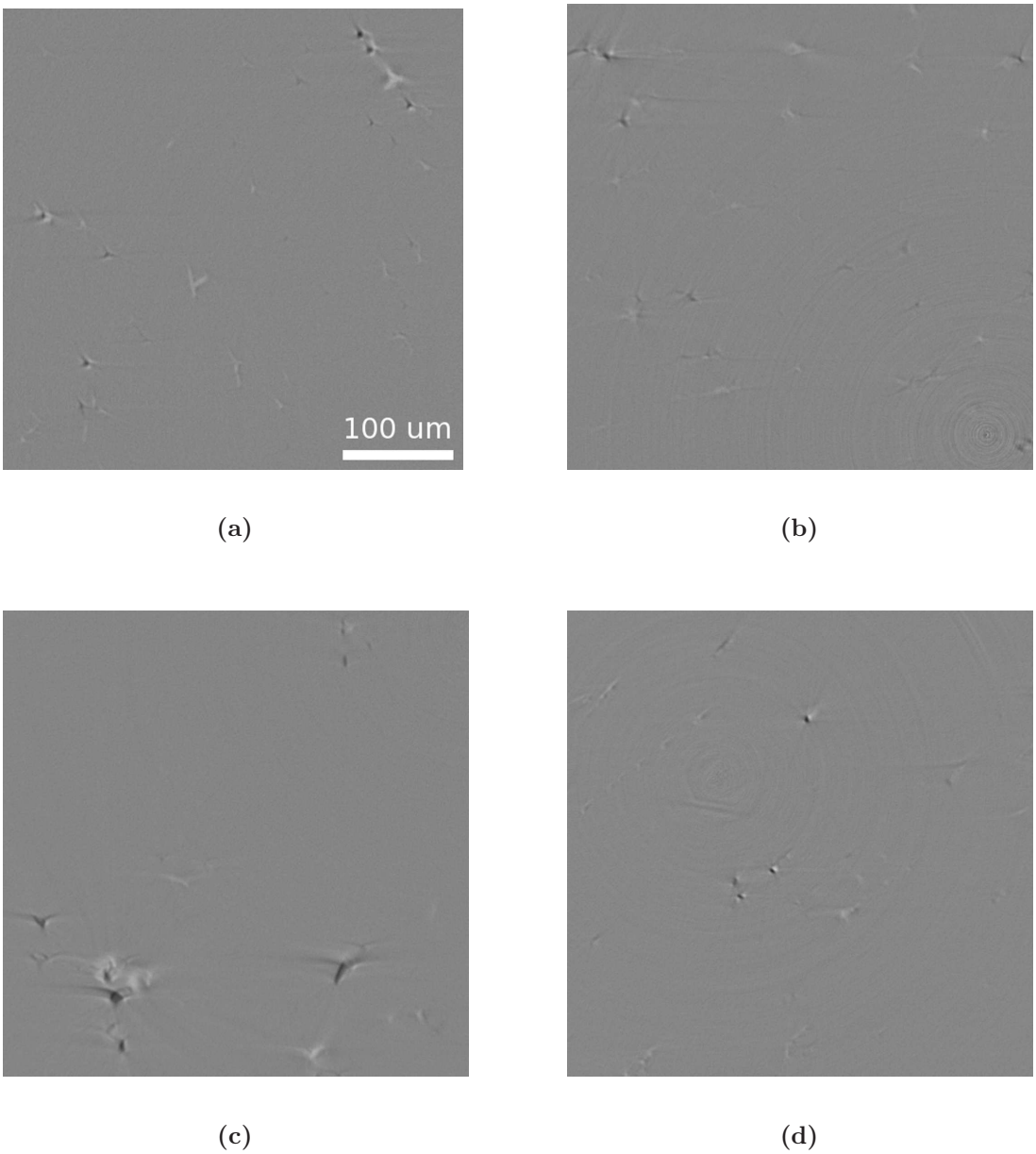

Figure 4.9. Reconstruction Artifacts: (a) NL3 Scan; (b) SL4 Scan; (c) SS6 Scan; (d) ST1 Scan.

Chapter 5

Conclusion

The Octopus software used for the reconstruction of the tomography data was the only one available to us [2]. It is very fast, as it can perform a reconstruction of a 5GB to 25GB data set from 20 minutes to 1 hour. The accuracy of the reconstruction may be good for qualitative analysis; but as our results show, it proves inadequate for quantitative analysis.

Nevertheless, we believe that the tools developed for quantitative and statistical analysis of tomographic data are robust and sound, and we plan to use them in the context of more accurate reconstructions.

Alternate, more accurate reconstruction methods exist, although they are more computationally expensive [7]. The scans were performed from July 13 to July 15 of 2010, and therefore there was no time available for research and implementation of alternate reconstructions schemes. Although we will continue to pursue the use of other, more powerful reconstruction methods, that effort will be beyond the scope of this project.

References

[1] URL `http://rsbweb.nih.gov/ij/`.

[2] URL `http://www.inct.be/en/software/octopus`.

[3] URL `http://www.paraview.org`.

[4] D.O. Adams, J.M. Moriarty, A.M. Gallegos, and D.F. Adams. The v-notched rail shear test. *Journal of Composite Materials*, 41(3):281–297, 2007.

[5] AH Delaney and Y Bresler. A fast and accurate Fourier algorithm for iterative parallel-beam tomography. *IEEE Transactions on Image Processing*, 5(5):740–753, MAY 1996. ISSN 1057-7149.

[6] MA Fischler and RC Bolles. Random Sample Consensus - A Paradigm for Model-Fitting with Applications to Image-Analysis and Automated Cartography. *Communications of The ACM*, 24(6):381–395, 1981. ISSN 0001-0782.

[7] Gabor T. Herman. *Fundamentals of Computerized Tomography: Image Reconstruction from Projections*. Springer, July 2009. ISBN 9781852336172.

[8] G. Jones. personal communication, 2010.

[9] T. Kaczynski, K. Mischaikow, and M. Mrozek. *Computational Homology*. Springer, 2004.

[10] R. Klette and A. Rosenfeld. *Digital Geometry*. Elsevier, 2004.

[11] W.Y Lu, M.F. Horstemeyer, J.S. Korellis, and D. Grishabar, R.B.and Mosher. High temperature sensitivity of notched aisi 304l stainless steel tests. *Theoretical and Applied Fracture Mechanics*, 30:139–152, 1998.

DISTRIBUTION:

1	George C. Johnson, University of California at Berkeley, Berkeley, CA 94720	
1	MS 9153	J.L. Handrock, 8200
1	MS 9161	W.R. Even, 8650
1	MS 9154	M.E. Gonzales, 8640
1	MS 9042	E.P. Chen, 8246
1	MS 9042	M.L. Chiesa, 8249
1	MS 9409	H. Jin, 8246
1	MS 9042	W.Y. Lu, 8246
1	MS 9042	J.W. Foulk III, 8246
1	MS 9042	T.J. Vogler, 8246
1	MS 9042	A.A. Brown, 8249
1	MS 9042	J.A.W. Crowell, 8249
1	MS 9042	J.J. Dike, 8249
1	MS 9042	A. Lindblad, 8249
1	MS 9404	A. Mota, 8246
1	MS 0899	Technical Library, 8944 (electronic copy)
1	MS 0123	D. Chavez, LDRD Office, 1011

Sandia National Laboratories